Generation and active manipulation of qubits in $LiNbO_3$-based integrated circuits

P. R. Sharapova[1], K. H. Luo[1], H. Herrmann[1], M. Reichelt[1], T. Meier[1], and C. Silberhorn[1]
[1]*Department of Physics and CeOPP, University of Paderborn, Warburger Strasse 100, D-33098 Paderborn, Germany*

We present and discuss perspectives on developing advanced quantum optical circuits monolithically integrated in the lithium niobate platform. A set of basic components comprising photon pair sources based on parametric down conversion (PDC), passive routing elements and active electro-optically controllable switches and polarisation converters are constituent parts of a toolbox which is the basis for a broad range of diverse quantum circuits. We discuss the state of the art of these components and present models that properly describe their performance in quantum circuits. As a demonstration of the applicability of these models we consider as an example an on-chip two-photon interference circuit comprising a PDC section for photon pair generation followed by an actively controllable modified Mach-Zehnder structure for detecting Hong-Ou-Mandel (HOM) interference. The performance of such a chip is simulated theoretically by taking even imperfections in the properties of the individual components into account.

arXiv:1704.03769v1 [quant-ph] 12 Apr 2017

I. INTRODUCTION

Recent research on quantum communication and information processing (QCIP) has proven that quantum mechanical effects can be applied to overcome classical performance limitations in the fields of communication security, metrology and computation. Future practical development of QCIP will strongly rely on the development of miniaturised and reliable optical components. Over the past several years complex integrated photonic circuits have already been demonstrated, which, for example, allow for the realisations of two-photon interference, CNOT-gate and path-entangled states of two photons [1], multi-photon quantum interference [2], the simulation of quantum Boson sampling [3] and quantum walk systems [4, 5]. These works have demonstrated the benefits of integrated solutions [6, 7] over bulk optical approaches in terms of stability, scalability, connectability and reproducibility. In addition, due to its on-chip nature and controllable capability, the miniaturised optical system represents a significant step forward for achieving integrated all-optical communication and optical computing systems.

However, the development of compact quantum optical circuits using waveguide components is still at a very early stage. The essential building blocks of such circuits are photon sources, passive and active elements to route and manipulate the photons and – in the ideal case – even single photon detectors. All these components with good performance properties have been demonstrated as single devices, but realised in different materials. Thus, nowadays it is still an open question which material platform is best suited for an integration of larger advanced quantum circuits [8].

$LiNbO_3$ is an attractive candidate serving as a platform for the development of advanced integrated quantum circuits. Besides its outstanding electro-optic, acousto-optic and nonlinear optic properties, mature and reliable waveguide fabrication techniques, e.g., by the in-diffusion of Titanium, exist, which is a basic prerequisite. On-chip generation and manipulation of qubits can harness the strong $\chi^{(2)}$-nonlinearity which can be specifically tailored by exploiting quasi-phase-matching (QPM) in periodically-poled waveguides [9]. For instance, photon pairs can be generated efficiently via parametric down-conversion (PDC). The exploitation of the versatile electro-optic properties of $LiNbO_3$ enables the manipulation of qubits (e.g. phase, polarisation, etc.) with bandwidths up to several GHz. But the full potential of $LiNbO_3$ has not yet been completely exploited. Various groups have demonstrated the photon-pair generation using type I or type II phase-matching in different configurations and different wavelength ranges [10–16].

Towards a more complex integration a few examples have recently been demonstrated; reviews can be found in [6, 17]. For example in [18] an efficient source of heralded single photons using a non-degenerate PDC followed by a passive directional coupler acting as wavelength selective splitter has been demonstrated. More advanced quantum circuits are a quantum relay chip [19] and a circuit for on-chip generation and manipulation of entangled photons [20], both of these examples already include active electrooptic components.

In this paper, we discuss design issues of advanced integrated quantum circuits in $LiNbO_3$. We briefly review the operational principles and the state-of-the-art of the elementary building blocks which are required for such circuits. We further derive models for a quantum optical description of these components. These models are not restricted to a description of the ideal performance of the individual elements but are able to take possible imperfections into account. As an example we discuss an on-chip two-photon interference circuit comprising a PDC stage for photon pair generation followed by an actively controllable modified Mach-Zehnder structure for Hong-Ou-Mandel (HOM)interference.

II. FUNCTIONAL ELEMENTS FOR QUANTUM CIRCUITS

In the past decades, a multitude of integrated optical devices in $LiNbO_3$ have been developed and demonstrated [21]. In particular, electro-optic modulators have become successful commercial products, which are dedicated for classical applications in telecommunications. Our vision is to benefit from these experiences and adapt them to the challenging demands required for quantum optical applications. A prerequisite for the development of advanced integrated quantum circuits in $LiNbO_3$ is a profound understanding and optimisation of the individual components forming such circuits.

The basis for the development of such devices is a reliable waveguide technology. Two mature waveguide fabrication techniques exists for integrated optical devices in $LiNbO_3$: proton-exchange and Ti-indiffusion. Both techniques enable the fabrication of single-mode waveguides with low losses (< 0.1 dB/cm). However, only the Ti-indiffusion technique provides guiding of waves in both orthogonal polarisations (TE and TM / H and V). Thus, for quantum circuits which exploit polarisation qubits the Ti-indiffusion technique is the preferred one.

We exploit this waveguide technology to discuss the design of different functional blocks to build up integrated quantum photonic devices forming a toolbox for application specific quantum circuits. The toolbox contains elements to generate and convert single photons or photon pairs via $\chi^{(2)}$-based nonlinear interactions, truly passive elements to route photons on-chip and electro-optic actively controllable elements for switching and polarisation conversion. In the following we discuss in detail the specific features of these different categories.

A. Photon Pair Sources

The development of telecom compatible, compact and reliable sources of entangled photons is a prerequisite to pave the way for most quantum optical experiments, either for fundamental research or even for a successful implementation of future quantum information technologies into real world applications. Therefore, the development of rugged and efficient photon (pair) sources to produce qubits is the first step. Photon pairs can be generated via PDC exploiting the $\chi^{(2)}$ nonlinearity of $LiNbO_3$ (Fig. 1).

Photon pair generation via PDC is governed by energy conservation and phasematching. The latter one requires a matching of the wave vector of the pump photon k_p with the wave vectors of the generated signal and idler photon $k_{s,i}$ according to:

$$k_p = k_s + k_i - \frac{2\pi}{\Lambda}, \tag{1}$$

where Λ is the period of the ferroelectric domain grating in the periodically-poled $LiNbO_3$ waveguide (PPLN). Via a proper choice of this poling period Λ the wavelengths at which phase-matching is fulfilled can be determined. Of course, Λ is fixed during the fabrication process. However, a fine tuning to the desired wavelength combination is usually possible by exploiting the temperature dependencies of the refractive indices.

Different phase-matched PDC processes can be exploited: Via a type I phase-matching, extraordinarily polarised signal and idler photons are created with by an extraordinarily (TM/H) polarised pump photon. This process uses the strong d_{33} nonlinear coefficient of $LiNbO_3$ and, thus, is very effective. However, for a process close to degeneracy, the spectral bandwidth is very broad (typically some 10 nm). Another option is a type II phase-matched process, where an ordinarily polarised pump generates a photon pair with orthogonal polarisation via a nonlinear coupling exploiting the d_{31} coefficient. The efficiency of this process is about $(d_{33}/d_{31})^2 \approx 40$ smaller, but the spectral bandwidth is also much narrower. Thus, the spectral densities of both processes are almost equal [15]. As a source of qubits preparation the

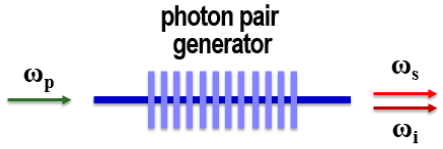

FIG. 1. Photon pair generation by parametric down-conversion (PDC) in a periodically-poled $LiNbO_3$ waveguide.

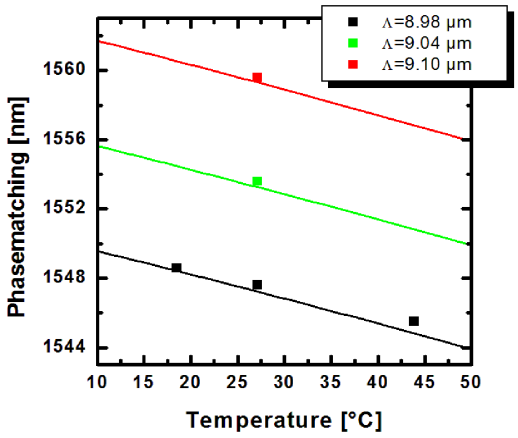

FIG. 2. Type II phasematched signal/idler wavelength for degenerate PDC in a Ti-indiffused waveguide in PPLN for various poling periods as function of the sample temperature. Solid lines: Calculated curves based on Sellmeier equations for $LiNbO_3$ [22, 23] and a waveguide dispersion derived using a Gauss-Hermite-Gauss approximation[24]. Symbols: Experimental data determined via second harmonic generation (SHG).

type II phase-matched degenerate PDC is in most cases preferable as it generates signal and idler photons with orthogonal polarisations which can be directly used to encode the information.

For a degenerate type II phase-matched PDC process to generate photon pairs in the telecom band poling periods around 9 μm are required. Details are shown in Fig. 2, where the phase-matching wavelength for degenerate PDC is plotted versus the sample temperatures for various poling periods. The calculated curves coincide very well with the experimental data.

Since for a type II degenerate PDC in a periodically-poled $LiNbO_3$ section with waveguiding achieved by Ti-indiffusion, the signal and idler photons of the photon pair have orthogonal polarisations, they have different group velocities in the waveguides. The biphoton state which is created in the PDC section can be described according to lowest-order perturbation theory by the following state vector [25]

$$|\psi_{PDC}\rangle = \int d\omega_s d\omega_i F(\omega_s,\omega_i) a^\dagger_{1H}(\omega_s) a^\dagger_{1V}(\omega_i)\,|0\rangle\,, \quad (2)$$

where $a^\dagger_{1H}(\omega_s)$ and $a^\dagger_{1V}(\omega_i)$ are the photon creation operators for the signal (idler) frequency modes which are horizontally and vertically polarised, respectively, and the index 1 corresponds to a particular spatial mode, later referred to as channel, in the waveguide system.

The two-photon amplitude (TPA) represents the probability amplitude of the creation of photons with frequencies ω_s and ω_i. For the PDC section pumped by a laser with a Gaussian envelope, $E_p^{(+)}(\mathbf{r},t) = E_0 e^{-\frac{t^2}{2\tau^2}} e^{i(\mathbf{k}_p\cdot\mathbf{r}-\omega_p t)}$, with a full width at half maximum (FWHM) of the intensity of $2\sqrt{\ln 2}\tau$, τ is a pulse duration, the TPA is given by

$$F(\omega_s,\omega_i) = C\exp[\frac{(\omega_s+\omega_i-\omega_p)^2}{2\Omega^2}]\mathrm{Sinc}[\frac{\Delta k\, L_{PDC}}{2}] \times \exp[\frac{i\Delta k\, L_{PDC}}{2}], \quad (3)$$

where C is the normalisation constant, $\Delta k = k_p(\omega_s+\omega_i) - k_s(\omega_s) - k_i(\omega_i) + \frac{2\pi}{\Lambda}$ is the wave vector mismatch inside the periodically-poled section, $\Lambda \approx 9$ μm is the poling period, L_{PDC} is the length of the PDC section and $\Omega = 1/\tau$. The signal and idler wave vectors $k_{s,i} = \frac{n_{s,i}(\omega_{s,i})\omega_{s,i}}{c}$ depend on the effective indices $n_{s,i}(\omega_{s,i})$ of the waveguide modes which can be calculated as $n_{s,i} = n_{s,i}^{LiNbO_3} + \delta n_{s,i}$. The first term is the bulk refractive index of $LiNbO_3$ which can be obtained by using the dispersive Sellmeier formulas [26]. To determine $\delta n_{s,i}$ the propagation constants of the respective waveguide modes must be calculated. This can be done using a numerical solver (e.g. a finite element based solver) applied to the refractive index profile of the Ti-diffused waveguide [27]. In most cases, however, much simpler almost analytical methods (e.g. Gauss-Hermite-Gauss approximation [24] or effective-index-methods [27]), provide sufficiently good results for a quantitative evaluation.

The TPA is mainly characterised by two parameters: the duration of the pump pulse and the length of the PDC section. Whereas the brightness of the PDC source increases with the length of the PDC section, and increased length simultaneously gives rise to a time delay between the orthogonally polarised photons since the PDC process predominantly takes place in the centre of the PDC section. This effect is included in our description by the last term in Eq. (4). Therefore, already at the end of the PDC section the two photons have accumulated a time delay determined by approximately their propagation with different velocities through half of the PDC section length.

The efficiency of the generation process depends on nonlinear optical coefficient, the overlap of the pump field mode with the signal and idler mode and on the interaction length. The overlap can be optimised by a proper design of the waveguide geometry and, hence, the waveguide fabrication. Detailed studies on optimised profiles have been performed for various classical nonlinear three wave mixing processes like second harmonic, sum- or difference frequency generation [28].

Several papers reported the application of such a type II phase-matched PDC process in Ti-indiffused PPLN waveguides for photon pair generation in the telecom band [12, 14, 15]. In a 30 mm long waveguide efficient pair generation within a spectral bandwidth <1 nm and a brightness of 6×10^5 pairs/(s mW GHz) has been demonstrated [15]. Such efficiencies are about two orders of magnitude larger compared to sources exploiting PDC in bulk crystals.

B. Passive Routing

Directional couplers are the basic elements for routing and splitting of the biphoton states. Such structures comprise a coupling region consisting of two closely adjacent waveguides in which a power exchange between these guides is possible. A proper design of this coupling region enables specific functionalities of the directional couplers. In Fig. 3 some examples are sketched.

To achieve the desired functionality the specific structure has to be determined. This includes size of the waveguides, separation of the waveguides in the coupling region, length of the coupling region and coupling in the branching regions. Several modelling tools for such directional couplers are available.

In the local normal mode description [29], the overall coupler is treated as a single waveguide with changing dimensions along the propagation direction. At least two eigenmodes - a symmetric and an antisymmetric - are guided in this structure. Launching a wave into one input port of the directional coupler will excite the two eigenmodes with equal amplitude. Assuming that all dimensional changes along the coupler structure are adiabatic, there is no coupling, i.e. power exchange, between these eigenmodes. But the propagation constants of the eigen-

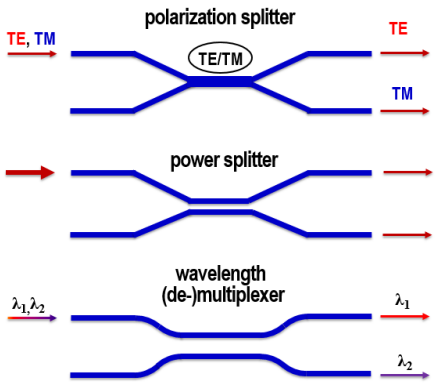

FIG. 3. Basic structure of the directional coupler with zero gap and large gap acting as integrated polarisation and/or power splitter and wavelength multiplexer.

modes along the structure may vary. The power splitting at the output of the coupler is a result of the interference of the two eigenmodes at the end of the structure. If the accumulated phase-difference between the even and odd eigenmodes is an even multiple of π, the power is routed to the bar-state output. For an odd multiple of π the power is coupled into the cross-state output.

An example of a directional coupler and its splitting performance is shown in Fig. 3. The coupler consists of a central section, in which the two incoming waveguides are merged to a single one with doubled width, i.e. there is no gap between the waveguides anymore (zero-gap coupler). The separation of the waveguides in the branching regions are done via inclined straight waveguides. The purpose of this device was to act as polarisation splitter (PBS). The branching angle and the length of the central coupling region was designed using the local normal mode method described above. The accumulated phase-difference of the eigenmodes is 2π for TE-polarised waves and 3π for TM-polarisation. Thus, TE waves are routed to the bar-state output and TM-waves to the cross-state output.

Afterwards, such structures were fabricated with a certain variation of the central section length. The splitting ratio is defined as the ratio of the power in the unwanted port to sum of the powers in both output ports. In Fig. 4 the measured splitting ratios for TE and TM are shown. It can be seen that the device really works as polarisation splitter if the central section length is about 500 μm. But the best splitting ratios for TE and TM occur at slightly different central section lengths. The optimum for TE is achieved with $L_c \approx 450$ μm whereas the ideal coupling for TM is at $L_c \approx 530$ μm. However, even with $L_c \approx 500$ μm a polarisation splitting better than 17 dB for both polarisations is obtained.

To describe the propagation of a biphoton state through such a polarisation splitter a unitary transformation can be applied. We can describe the corresponding

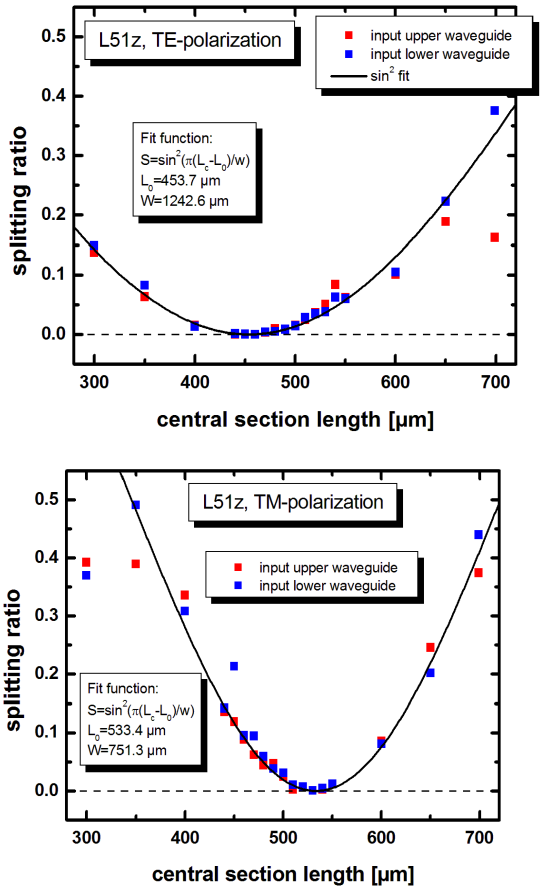

FIG. 4. Measured splitting ratios of sample L51z (name of the sample) as function of the central section length by using the narrow band laser $\lambda_p = 1550$ nm. Additionally, a $\sin^2$-fit function to the data is shown. Please note that the experimental data are shown with error bars smaller than symbol size.

transformation matrix of the PBS element in the basis $\{a^\dagger_{1H}(\omega_{s,i}), a^\dagger_{1V}(\omega_{s,i}), a^\dagger_{2H}(\omega_{s,i}), a^\dagger_{2V}(\omega_{s,i})\}$, where the index $\{1,2\}$ denotes the channel number and $\{H,V\}$ the polarisation, is given by

$$PBS = \begin{pmatrix} i\sin\alpha & 0 & \cos\alpha & 0 \\ 0 & i\cos\beta & 0 & \sin\beta \\ \cos\alpha & 0 & i\sin\alpha & 0 \\ 0 & \sin\beta & 0 & i\cos\beta \end{pmatrix}. \qquad (4)$$

Here, the angle α describes the transformation of the horizontally-polarised photons and the angle β corresponds to the vertically-polarised photons. The PBS element works perfect for $\alpha = \beta = \pi/2$ and in this case the horizontally-polarised mode is transmitted in the upper channel 1 and the vertically-polarised mode in the lower channel 2, respectively. The consideration of two angles α and β allows us to describe different imperfect polarisation splitting for TE and TM. The matrix is the

same for the signal and idler frequencies as long as the photon pair generation is close to degeneracy and, thus, the wavelength dependence of the PBS can be neglected.

The beam splitter (BS) for power splitting or wavelength multiplexing is usually obtained by using a directional coupler with large gap and S-shaped bends consisting of circular arcs. The central gap separation, bending radius and central section length has to be optimised to provide the desired purpose. As soon as the coupler is fabricated with designed parameters, its splitting behaviour is fixed passively.

For taking imperfections in the different channels of the BS into account we introduce two angles θ (for the upper channel) and ξ (for the lower channel) and define the BS transformation by

$$BS = \begin{pmatrix} \cos\theta & 0 & i\sin\theta & 0 \\ 0 & \cos\xi & 0 & i\sin\xi \\ i\sin\theta & 0 & \cos\theta & 0 \\ 0 & i\sin\xi & 0 & \cos\xi \end{pmatrix}. \qquad (5)$$

As mentioned above, the BS matrix is the same for the signal and idler frequencies.

C. Active Electrooptic Manipulation

An outstanding feature of $LiNbO_3$ is its capability of electrooptic modulation which enables on-chip manipulation of optical waves via externally applied control voltages. These electrooptic properties have been widely used to develop various versions of e.g. integrated intensity modulators or phase-shifters. Obviously, the exploitation of electrooptic manipulation of optical waves offers also a huge potential for the design and realisation of advanced integrated quantum circuits. Examples for such electro-optic devices for active manipulation of the quantum state are given schematically in Fig. 5.

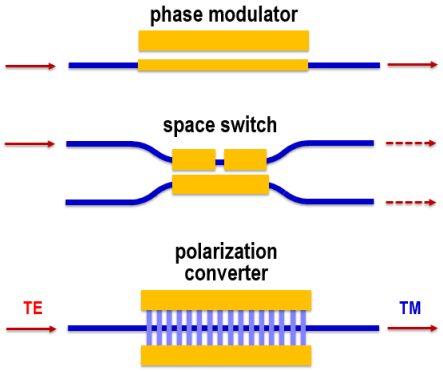

FIG. 5. Basic structures of the active manipulation in the integrated waveguides.

1. *Phase modulators*

The simplest electro-optic device is a phase-modulator which comprises an optical waveguide within an electric field. This field is generated via a voltage applied to electrodes. For a phase-modulator in z-cut $LiNbO_3$ one electrode is placed on top of the waveguide (but separated from the waveguide with a dielectric buffer layer) and a second electrode besides the waveguide. A voltage applied to the electrodes generates an electrical field which is predominantly oriented along the crystalline z-direction in the waveguide region. The phase of a TM-polarised wave is modulated by the electric field via the strong electro-optic coefficient r_{33} whereas TE-polarised waves are modulated via r_{31}. As the latter coefficient is about a factor of three smaller, the overall device performance yields a differential phase-modulation.

Due to the fact that the phase modulator changes the phase of the vertically and horizontally polarised modes differently, the matrix of phase modulator placed in one spatial channel is:

$$PM = \begin{pmatrix} \exp[i\Phi_H] & 0 & 0 & 0 \\ 0 & \exp[i\Phi_V] & 0 & 0 \\ 0 & 0 & 1 & 0 \\ 0 & 0 & 0 & 1 \end{pmatrix}, \qquad (6)$$

where Φ_H and Φ_V are the additional phase for the horizontally and vertically polarised modes.

2. *Electro-optically adjustable beam splitters*

Variable beam-splitters are key components for various quantum applications which require any kind of dynamic spatial routing or switching or solely a fine-tuning of the splitting ratios. For such demands, electro-optical beam splitters are best suited as they can provide a flexible operation even at high bandwidths, which in principle can go up to several GHz.

The basis of such electro-optic splitters are again directional couplers but equipped with proper electrodes for the electro-optic driving. The most flexible configuration is based on a so called $\Delta\beta$-reversal scheme as sketched in Fig. 6 [30]. Usually, a structure with a relatively large gap between the waveguides in the coupling region is chosen. Thus, the weak coupling leads to a longer coupling length, which is required to provide sufficient interaction length for the electro-optic modulation. The electrode configuration is sketched in Fig. 6. Electrodes are above the two optical waveguides but separated via a dielectric buffer layer. Above one waveguide the electrode is split in two parts, which allows to apply two different voltages U_1 and U_2. Such an electrode scheme allows to compensate even if some inhomogeneities - like for instance a slight mismatch of the width of the two waveguides in the coupling section – are present. By a proper choice

of the two voltages a perfect switching between the bar- and the cross-state output ports is possible.

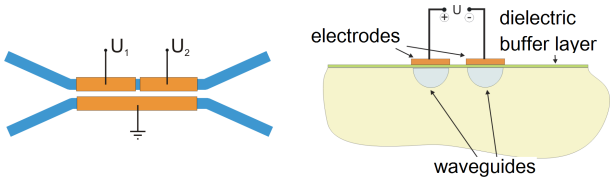

FIG. 6. Schematics of electro-optical switch comprising of a directional coupler with $\Delta\beta$-reversal electrodes. Left: Top view, right: cross-sectional view in the coupling region.

In Fig. 7 an experimentally determined switching characteristics of such a directional coupler. The coupler has a central coupling length of 8 mm and is was characterised by launching TM-polarised light at $\lambda \approx 1550$ nm into one input port of the device. In the diagram the normalised transmission at the bar-state output is shown as function of the two voltages. It can clearly be seen that all possible splitting ratios can be adjusted by a proper choice of the voltages.

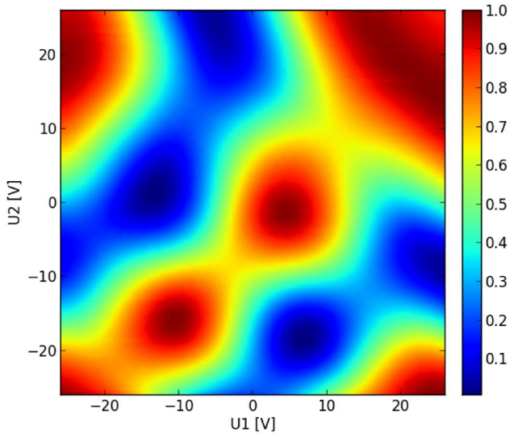

FIG. 7. Measured (normalised) bar state output power as function of the applied voltages U_1 and U_2 of an electro-optically adjustable beam-splitter consisting of a directional coupler with an 8 mm long coupling region.

For the modelling of the quantum circuits such electro-optically adjustable beam splitter are described by the usual beam splitter matrix Eq. (5). The two angles θ and ξ of course depend on the applied voltages U_1 and U_2.

3. *Electro-optic polarisation converter*

In the electro-optic polarisation converter the polarisation state can be changed by applying a voltage. This can be obtained using an electrooptically induced coupling between TE- and TM-polarised modes via the r_{51} element of the electrooptic tensor. The schematic structure of such an integrated polarisation converter is shown in Fig. 5 [31, 32]. It consists of a Ti-diffused waveguide within a periodically-poled section with a poling period Λ_{PC}. Adjacent to both sides of the waveguides are electrodes deposited on the sample, i.e. an voltage U applied to the electrodes leads to an electrical field mostly pointing along the crystalline $Y-$direction in the waveguide region, which gives rise to the TE-TM coupling. Note, however that this process requires phase-matching as well. The corresponding phase-matching condition is given by:

$$\Delta k_{PC} = \frac{2\pi}{\lambda}\left(n_{\mathrm{TE}}(\lambda) - n_{\mathrm{TM}}(\lambda)\right) - \frac{2\pi}{\Lambda_{PC}} \qquad (7)$$

with $n_{\mathrm{TE/TM}}$ being the effective indices of the TE- and TM-mode, respectively. Similar to nonlinear optical interactions, this phase-matching requirement leads to a spectral dependence. A perfect conversion is happened for $\Delta k_{PC} \approx 0$.

The efficiency of the conversion process is determined by the overlap between the optical fields and the electric field component along the crystalline Y-axis. As the field strength scales linear with the applied voltage, the coupling coefficient κ is proportional to U. The TE-TM conversion process can easily be described using standard coupled mode theory. Assuming that $A_{\mathrm{TE}}(0)$ and $A_{\mathrm{TM}}(0)$ are the amplitudes of the waveguide modes in TE and TM polarisation in front of the converter, these amplitudes evolve in the converter section according to:

$$\begin{aligned} A_{\mathrm{TE}}(z) &= \left\{ A_{\mathrm{TE}}(0)\left[\cos sz - i\frac{\Delta\beta}{2s}\sin sz\right] \right. \\ &\quad \left. -i\frac{\kappa}{s}A_{\mathrm{TM}}(0)\sin sz \right\} \exp\left(i\frac{\Delta\beta z}{2}\right) \\ A_{\mathrm{TM}}(z) &= \left\{ A_{\mathrm{TM}}(0)\left[\cos sz + i\frac{\Delta\beta}{2s}\sin sz\right] \right. \\ &\quad \left. -i\frac{\kappa}{s}A_{\mathrm{TE}}(0)\sin sz \right\} \exp\left(-i\frac{\Delta\beta z}{2}\right) \end{aligned} \qquad (8)$$

with

$$s = \sqrt{\kappa^2 + \left(\frac{\Delta\beta}{2}\right)^2} \qquad (9)$$

Such polarisation converters have been fabricated and experimentally characterised. In Fig. 8 a measured spectral characteristics is shown. The curves have been obtained using a 7.6 mm long structure with a poling period of $\Lambda = 21.4$ μm. Spectra for different applied voltages are given. Complete conversion is obtained with a driving voltage of $U = 25.5$ V. The shape of the spectra show the predicted sinc^2-behaviour with $\Delta\lambda \approx 3.2$ nm full width at half maximum (FWHM). Please note, that the spectral width is determined by the interaction length L. From Eq. (8) it can easily be derived that the FWHM

is proportional to $1/L$. Thus, spectral bandwidth as well as matching of a central frequencies of all the elements on a circuit is a crucial design parameter, which has to be under full control in the abreaction processes and the experimental quantum optical setups.

From the results shown in Fig. 8, it is remarkable that even for $U = 0$ V some conversion can be observed. Obviously, this is due to some residual stress in the sample (which most probably arise during the periodic poling). Such stress can build up internal electric fields giving rise to the observed conversion. At an applied voltage of $U \approx 5.5$ V the conversion almost completely vanishes indicating that the internal fields are compensated by the field produced due to the applied voltage.

At perfect phase-matching the conversion efficiency can be tuned between 0 and 1 by adjusting the voltage. A corresponding measurement result is shown in Fig. 9, where we varied the voltage and measured the unconverted power. As predicted from the theory (Eq. (8)), we could clearly observed the $\sin^2$-behaviour.

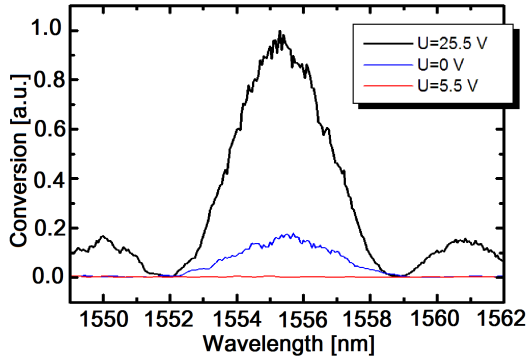

FIG. 8. Phase matching characterisation of periodic poling of the electrooptic polarisation converter. Measurements have been performed in a 7.5 mm long polarisation converter with $\lambda_{PC} = 21.4$ μm.

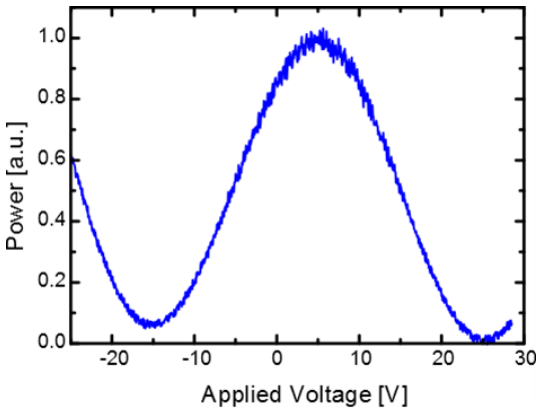

FIG. 9. Unconverted power vs applied voltage at phase matched wavelength.

For the modelling of the polarisation converter (PC) we describe the action of the PC in the basis $\{a^\dagger_{1H}(\omega_{s,i}), a^\dagger_{1V}(\omega_{s,i}), a^\dagger_{2H}(\omega_{s,i}), a^\dagger_{2V}(\omega_{s,i})\}$ by a transformation matrix which depends on phasematching condition [33]

$$PC = \begin{pmatrix} \cos\phi + ia\sin\phi & -b\sin\phi & 0 & 0 \\ b\sin\phi & \cos\phi - ia\sin\phi & 0 & 0 \\ 0 & 0 & 1 & 0 \\ 0 & 0 & 0 & 1 \end{pmatrix}, \quad (10)$$

where $a = \frac{\frac{\Delta k_{PC}}{2}}{\sqrt{\kappa^2+(\frac{\Delta k_{PC}}{2})^2}}$, $b = \frac{\kappa}{\sqrt{\kappa^2+(\frac{\Delta k_{PC}}{2})^2}}$. $\phi = \sqrt{\kappa^2 + (\frac{\Delta k_{PC}}{2})^2} L_{PC}$ is the angle of polarisation conversion and L_{PC} is the length of the polarisation converter. For $\kappa = \frac{\pi}{2L_{PC}}$ and perfect phase matching $\Delta k_{PC} = 0$ one obtains a complete conversion, i.e. $\phi = \pi/2$. In this case the polarisation is switched from horizontal to vertical and vice versa, $\phi = 0$ corresponds to a non-converted case. The PC matrix is the same for the signal and the idler photons. It is important to note that since the PC depends on the phasematching condition, the corresponding matrix is intrinsically frequency dependent and resulting from this frequency dependence, conversion happens only in a narrow wavelength range where $\Delta k_{PC} \approx 0$. This means that the spectral shape of PDC photons must belong to this conversion region, otherwise imperfect conversion efficiency will occur. A window of conversion for a poling period of $\Lambda_{PC} \approx 21.4$ μm is defined by the absolute value squared of the matrix element $|-b\sin\phi|^2$ and shown in Fig. 10. With increasing PC section length the window of conversion gets narrower which may result a degraded conversion efficiency.

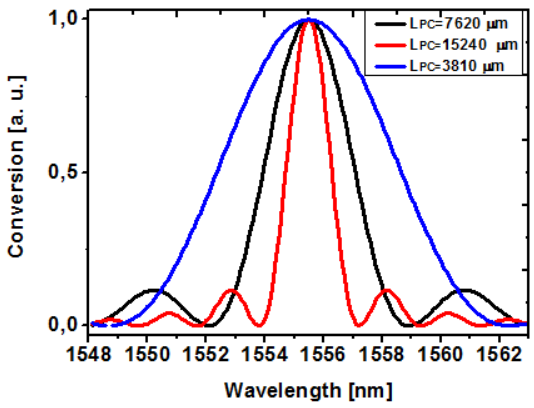

FIG. 10. A window of conversion for different length of PC, theoretical calculation: 3810 μm (blue), 7620 μm (black) and 15240 μm (red).

III. ADVANCED CIRCUIT EXAMPLE

The functional components discussed in the previous section can be used to construct complex integrated circuits. To demonstrate the practicality of combinations of all components, we present in this section a specific example, which can be considered as a benchmark system. We show, how it is possible to design a circuit with a desired functionality and how the modelling tools can be applied to predict device performance. In our example, we choose a circuit which includes a PDC-based photon-pair source and an asymmetric Mach-Zehnder like interferometer structure giving rise to HOM quantum interference.

In Fig. 11 the structure of the monolithic quantum optical waveguide chip is sketched schematically. Along with described above optical elements this chip includes the free propagation sections which are described by free propagation matrices. Each free propagation matrix has the form

$$FP = \begin{pmatrix} \exp[i\frac{\omega_s}{v_H}l_1] & 0 & 0 & 0 \\ 0 & \exp[i\frac{\omega_s}{v_V}l_1] & 0 & 0 \\ 0 & 0 & \exp[i\frac{\omega_s}{v_H}l_2] & 0 \\ 0 & 0 & 0 & \exp[i\frac{\omega_s}{v_V}l_2] \end{pmatrix}, \tag{11}$$

where $v_H = c/n_H(\omega_s)$ and $v_V = c/n_V(\omega_s)$, n_H, n_V are the refractive indices for horizontally, vertically-polarised light, c is the speed of light in vacuum and l_1 and l_2 are the lengths of the free propagation in the upper channel 1 and the lower channel 2, respectively.

First, spectrally degenerate photon pairs at telecom wavelengths are generated via type II phase-matched PDC. The orthogonally-polarised photons of the generated pairs are spatially separated by a PBS. By a polarisation converter the polarisation of one photon is rotated by 90^o. Due to the different group velocities there is a time delay between the photons in the various components of the chip, which can be compensated by different optical path lengths of the upper and lower branch in the subsequent part of the Mach-Zehnder interferometer. Then, both photons of the pair are routed to the input port of a directional coupler acting as a BS. In this BS the two photons, which are now indistinguishable with respect to frequency, polarisation and time, interfere, which results in bunching according to the HOM effect.

A. Theoretical Description

The total transformation matrix for the setup sketched in Fig. 11 has the form

$$U_{total} = BS * FP_3 * PC * FP_2 * PBS * FP_1, \tag{12}$$

where FP_1 corresponds to the free propagation between the end of the PDC section to the centre of the PBS

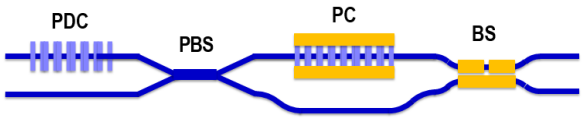

FIG. 11. Schematical illustration of a possible implementation of the complete circuit. Proposed integrated quantum optical chip with monolithically integrated PDC-source, polarisation splitter (PBS), electrooptic polarisation controller (e/o-PC) and interferometer beam splitter (BS).

(lengths $l_1 = l_2 = y$), FP_2 from the centre of the PBS to the centre of the PC (length $l_1 = l$ for the upper channel and $l_2 = L = l + \Delta l$ for the lower one), and FP_3 from the centre of the PC to the centre of the BS (lengths $l_1 = l_2 = z$). The free propagation from the BS to the detectors could also be included by considering an additional FP-matrix, however, since we consider in the following the detection of two photons with identical polarisation this would just lead to an unimportant overall phase factor if the propagation lengths to each of the two detectors are identical.

Due to the polarisation-dependent group velocities of the photons the compensation of the time delay can be performed by bringing an additional length to the second channel $L = l + \Delta l$. The same free propagation matrix applies also to the idler photons when ω_s is changed into ω_i.

The matrix U_{total} describes the transformation between the input and the output states. In the basis $\{a^\dagger_{1H}, a^\dagger_{1V}, a^\dagger_{2H}, a^\dagger_{2V}\}$ the input state, see Eq. (2), can be represented by

$$|\psi_{PDC}\rangle = \int d\omega_s d\omega_i F(\omega_s, \omega_i)$$
$$U_0(\omega_s) \begin{pmatrix} a^\dagger_{1H}(\omega_s) \\ a^\dagger_{1V}(\omega_s) \\ a^\dagger_{2H}(\omega_s) \\ a^\dagger_{2V}(\omega_s) \end{pmatrix} \otimes U_0(\omega_i) \begin{pmatrix} a^\dagger_{1H}(\omega_i) \\ a^\dagger_{1V}(\omega_i) \\ a^\dagger_{2H}(\omega_i) \\ a^\dagger_{2V}(\omega_i) \end{pmatrix} |0\rangle\,, \tag{13}$$

where

$$U_0(\omega_s) = \begin{pmatrix} 1 & 0 & 0 & 0 \\ 0 & 0 & 0 & 0 \\ 0 & 0 & 0 & 0 \\ 0 & 0 & 0 & 0 \end{pmatrix}, \quad U_0(\omega_i) = \begin{pmatrix} 0 & 0 & 0 & 0 \\ 0 & 1 & 0 & 0 \\ 0 & 0 & 0 & 0 \\ 0 & 0 & 0 & 0 \end{pmatrix}, \tag{14}$$

are required to properly describe the photon pair generated in the type II PDC process.

The output state is defined by action of the total transformation matrix on the signal and idler subsystems. However, the measuring procedure is performed on the output operators. Thus we have to use the reverse transformation and express the initial operators in Eq. (13)

through the final ones, i.e.,

$$\begin{pmatrix} a^{\dagger}_{1H}(\omega_s,i) \\ a^{\dagger}_{1V}(\omega_s,i) \\ a^{\dagger}_{2H}(\omega_s,i) \\ a^{\dagger}_{2V}(\omega_s,i) \end{pmatrix} = U^{\dagger}_{total}(\omega_{s,i}) \begin{pmatrix} f^{\dagger}_{1H}(\omega_s,i) \\ f^{\dagger}_{1V}(\omega_s,i) \\ f^{\dagger}_{2H}(\omega_s,i) \\ f^{\dagger}_{2V}(\omega_s,i) \end{pmatrix}, \quad (15)$$

where $f^{\dagger}$ and f are the output creation and annihilation operators which describe the photons after the action of the final BS, i.e., directly before reaching the detectors. Substituting Eq. (15) in Eq. (13) we can write the output state as

$$|\psi_{out}\rangle = \int d\omega_s d\omega_i F(\omega_s,\omega_i) U_0(\omega_s) U^{\dagger}_{total}(\omega_s) \begin{pmatrix} f^{\dagger}_{1H}(\omega_s) \\ f^{\dagger}_{1V}(\omega_s) \\ f^{\dagger}_{2H}(\omega_s) \\ f^{\dagger}_{2V}(\omega_s) \end{pmatrix} \otimes U_0(\omega_i) U^{\dagger}_{total}(\omega_i) \begin{pmatrix} f^{\dagger}_{1H}(\omega_i) \\ f^{\dagger}_{1V}(\omega_i) \\ f^{\dagger}_{2H}(\omega_i) \\ f^{\dagger}_{2V}(\omega_i) \end{pmatrix} |0\rangle . \quad (16)$$

The total transformation matrix for the signal frequency can be represented in the form

$$U_{total}(\omega_s) = \begin{pmatrix} A^{HH}_{11} & A^{VH}_{11} & A^{HH}_{21} & A^{VH}_{21} \\ A^{HV}_{11} & A^{VV}_{11} & A^{HV}_{21} & A^{VV}_{21} \\ A^{HH}_{12} & A^{VH}_{12} & A^{HH}_{22} & A^{VH}_{22} \\ A^{HV}_{12} & A^{VV}_{12} & A^{HV}_{22} & A^{VV}_{22} \end{pmatrix}, \quad (17)$$

where $A^{\lambda\lambda^{'}}_{nn^{'}}$ is the matrix element corresponding to the transition $n\lambda \rightarrow n^{'}\lambda^{'}$. A similar matrix can be written for the idler frequency with coefficients denoted by $B^{\lambda\lambda^{'}}_{nn^{'}}$. Altogether, the output state is given by

$$|\psi_{out}\rangle = \int d\omega_s d\omega_i F(\omega_s,\omega_i) \sum_{n,\mu} A^{H\mu}_{1n}(\omega_s) f^{\dagger}_{n,\mu}(\omega_s) \times \sum_{n^{'},\mu^{'}} B^{V\mu^{'}}_{1,n^{'}}(\omega_i) f^{\dagger}_{n^{'},\mu^{'}}(\omega_i) |0\rangle , \quad (18)$$

where $n, n^{'} = \{1,2\}$ are the channel numbers and $\mu, \mu^{'} = \{H,V\}$ are the polarisation indices. $A^{H\mu}_{1n}(\omega_s)$ and $B^{V\mu^{'}}_{1,n^{'}}(\omega_i)$ are the coefficients which depend on the action of the optical elements $\phi, \theta, \xi, \alpha, \beta$ and on the lengths of the free propagations.

Measuring the coincidence probability at the detectors corresponds to calculating the expectation value of simultaneous positive-operator valued measures (POVM)

$$P^{\lambda,\lambda^{'}}_{b,c} = \langle \psi_{out}| M^{\lambda}_{b} \otimes M^{\lambda^{'}}_{c} |\psi_{out}\rangle , \quad (19)$$

where the POVM operators are given by

$$M^{\lambda}_{b} = \int d\omega_b d^{\dagger}_{1,\lambda}(\omega_b) |0\rangle \langle 0| d_{1,\lambda}(\omega_b), \quad (20)$$

$$M^{\lambda^{'}}_{c} = \int d\omega_c d^{\dagger}_{2,\lambda^{'}}(\omega_c) |0\rangle \langle 0| d_{2,\lambda^{'}}(\omega_c). \quad (21)$$

Here $d^{\dagger}_{1,\lambda}(\omega_b)$ and $d^{\dagger}_{2,\lambda^{'}}(\omega_c)$ are the creation operators of two detectors labeled as b and c and λ and $\lambda^{'}$ are the polarisations which are measured by the detectors b and c, respectively. We assume that detector b corresponds to the upper channel 1 and detector c to the lower channel 2. After a transformation the coincidence probability can be written in the simpler form

$$P^{\lambda,\lambda^{'}}_{b,c} = \int d\omega_b d\omega_c |\langle 0| d_{1,\lambda}(\omega_b) d_{2,\lambda^{'}}(\omega_c) |\psi_{out}\rangle|^2. \quad (22)$$

Substituting the output state, Eq. (18), in Eq. (22) and taking into account the commutation relation for the operators $[d_{n,\lambda}(\omega_b), f^{\dagger}_{n^{'},\mu}(\omega_s)] = \delta_{n,n^{'}}\delta_{\lambda,\mu}\delta(\omega_b - \omega_s)$ we obtain the following expression for the expectation value of simultaneous POVM

$$P^{\lambda,\lambda^{'}}_{b,c} = \int d\omega_b d\omega_c |F(\omega_b,\omega_c) \times \delta_{1,n}\delta_{\lambda,\mu} A^{H\mu}_{1n}(\omega_b) \delta_{2,n^{'}}\delta_{\lambda^{'},\mu^{'}} B^{V\mu^{'}}_{1,n^{'}}(\omega_c) + F(\omega_c,\omega_b)\delta_{1,n^{'}}\delta_{\lambda,\mu^{'}} B^{V\mu^{'}}_{1,n^{'}}(\omega_b)\delta_{2,n}\delta_{\lambda^{'},\mu} A^{H\mu}_{1n}(\omega_c)|^2. \quad (23)$$

For the case of polarisation insensitive detectors, which we do not consider below, the expectation value of the POVM corresponds to the sum of Eq. (22) over the all polarisation combinations, i.e.,

$$P^{ins}_{b,c} = \sum_{\lambda,\lambda^{'}} P^{\lambda,\lambda^{'}}_{b,c} . \quad (24)$$

Below we evaluate the dependence of the coincidence probability on the length difference of the upper and lower channels. To vary this length difference experimentally one could use an external delay line, which would, however, mean that one leaves the fully-integrated design. Alternatively, one may implement a kind of discrete delay line also in the integrated design by adding several switchable spatially-separated PCs in one channel and taking advantage of the different group velocities of horizontally- and vertically-polarised photons.

B. Dependence of the Hong-Ou-Mandel Interference Parameters and Imperfections

For the case of an ideal integrated device as sketched in Fig. 11, the generated two photons become fully indistinguishable when they reach the BS. Modifying the time delay between the photons, by, e.g. changing the length

of the lower channel, changes the coincidence probability of the photons measured in the detectors. If this time delay equals zero, the two photons are fully indistinguishable and the coincidence probability drops down close to zero, see Fig. 12. By increasing the time delay the photons become partially distinguishable and the coincidence probability increases and reaches 0.5 in the limit of a large time delay when the photons are totally distinguishable.

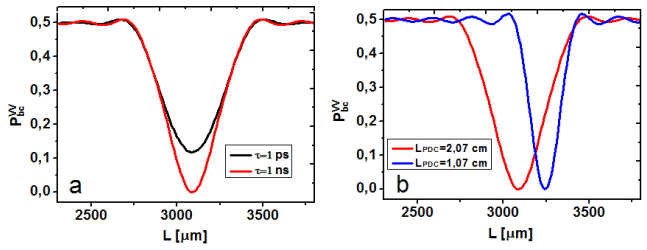

FIG. 12. The HOM dip as measured by the coincidence probability for detecting two vertically-polarised photons in the detectors for a perfect chip as sketched in Fig. 11. (a) Considering two pump pulse durations: $\tau = 1$ ns (red curve) and $\tau = 1$ ps (black curve) for the same length of the PDC section $L_{PDC} = 2.07$ cm, (b) Considering two PDC section lengths: $L_{PDC} = 1.07$ cm (blue curve) and $L_{PDC} = 2.07$ cm (red curve) for the same pulse duration ($\tau = 1$ ns)

A typical profile of the HOM dip is depicted in Fig. 12. This figure presents the expectation value of the POVM with $\lambda, \lambda^{'}$ both equal to V corresponding to two vertically-polarised photons and fully ideal optical elements. The HOM profile depends on the structure of the TPA function.

Fig. 12(a) visualises the dependence of the HOM dip on the duration of the pump pulse. In general, the TPA given by Eq. (4) is not fully symmetrical with respect to the exchange of the signal and idler variables due of the different refractive indices for the horizontally- and vertically-polarised light. If, however, the pulse duration is sufficiently long the TPA becomes very narrow in the $\omega_s = \omega_i$ direction and in this case the TPA becomes very close to a symmetrical function. This means that the minimum of the HOM dip will be very close to zero. For shorter pulse duration the non-symmetrical character of the TPA becomes more evident which leads to an increased value of the minimum of the coincidence probability.

With increasing length of the PDC section, see Fig. 12(b), the TPA becomes narrower in the frequency domain and consequently the HOM dip becomes broader in the time domain. Simultaneously the position of the HOM dip is shifted in length due to the increasing time delay between the photons accumulated already in the PDC section. This dependence on the length of the PDC section arises since the photon pairs are predominantly generated in the centre of the PDC section as modeled by the imaginary exponent in Eq. (4).

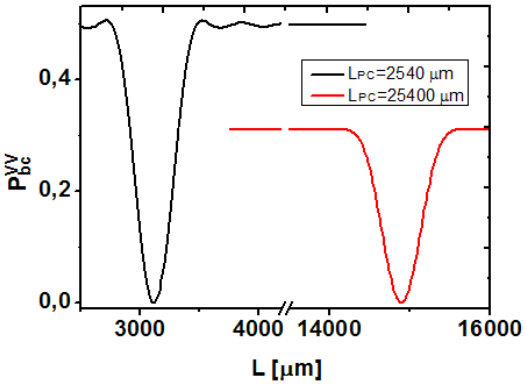

FIG. 13. The frequency dependence of the HOM dip is connected with the length of the PC. The HOM dip for $L_{PC} = 2540$ μm (black curve) and $L_{PC} = 25400$ μm (red curve). With increasing length of the PC the window of conversion gets narrow. That leads to worse conversion of side frequencies in the TPA,the HOM dip becomes broader, the maximum value decreases.

In a real device the considered optical elements will typically not work perfectly but their operation characteristics might deviate from the ideal case due to the limited accuracy of the fabrication process. In addition, also a certain degree of losses arising, e.g., from bending the waveguides or from the contacts that are required to apply the voltage, will be present. In our work, we neglect the losses since they can be kept on a very low level using available technology for the fabrication of waveguides in $LiNbO_3$ by Ti-indiffusion and in the following study imperfections of the optical elements, i.e., of the PBS, the PC and the BS. It is very important to know the limit of imperfections of the different optical elements until which quantum effects in the coincidence probability are still observable which corresponds to a minimum of the HOM dip smaller than the classical limit of 0.25.

With respect to imperfections and losses the most sensitive considered optical element is the PC. The PC has a window of conversion which corresponds to a principal limitation of the conversion efficiency for a fixed TPA profile. As usual the length of the PC is chosen such that the window of conversion is significantly broader than the spectral width of the TPA providing a good conversion, see black curve in Fig. 13. Hoewever, with increasing the length of the PC the window of conversion gets narrower which leads to non-perfect conversion of side frequencies and broadening of the HOM dip; simultaneously, the maximal value of coincidence probability decreases, see red curve in Fig. 13.

The modifications of the HOM curves due to imperfections are different for each of the optical elements. The profiles of the HOM dip with 25% imperfections are presented for the case of the BS in Fig. 14(a), the PBS in Fig. 14(b) and the PC in Fig. 14(c), respectively. In

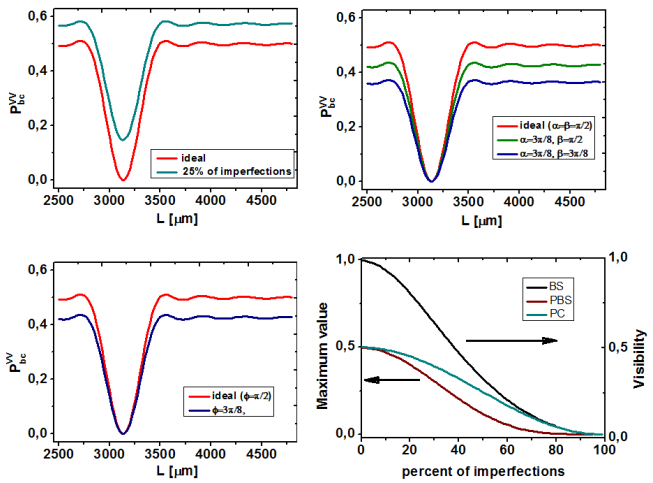

FIG. 14. The influence of imperfections of different elements on the coincidence probability. In (a)-(c) the red curves corresponds to the ideal case, whereas in the other curves 25% of imperfections in (a) the BS, (b) the PBS (here the green curve corresponds to the 25% of imperfections for only one polarisation whereas the blue curve is calculated for 25% of imperfectinos for both polarisations), (c) the *PC*. (d) The visibility as function of the BS imperfections (black curve) and the maximum values of the coincidence probability as function of the PBS (red curve) and the *PC* (cayan curve) imperfections.

Fig. 14(a)-(c) the red curves correspond to the ideal case when all optical elements work perfectly and in each figure we include imperfections of only a single optical element and assume that the other ones work perfectly. 25% of imperfections is defined in relation to the entire range of the respective angle which describes the element's operation. For example, the range of the BS is $\theta = [0, \pi/4]$, where $\theta = \pi/4$ corresponds to the perfect case of a 50/50 beam splitter and $\theta = 0$ to the totally imperfect case when light is just transmitted by the BS without any reflection. Therefore, 25% of imperfections means that $\theta = 3\pi/16$. Analogously, for the PBS and PC the range of definitions are $\phi = [0, \pi/2]$ and $\alpha, \beta = [0, \pi/2]$ and therefore 25% imperfections corresponds to $\phi = \alpha = \beta = 3\pi/8$ (in the case of PC this value of imperfections corresponds to the perfect phase matching condition $\Delta k_{PC} = 0$).

Fig. 14(a) shows that with imperfections of the BS the coincidence probability goes up and thus the HOM dip is weakened. In the totally imperfect case, i.e., when the BS has 100% transmission and 0% reflection, the coincidence probability goes to 1. Fig. 14(b) and (c) present the effects of imperfections in the PBS and in the PC. In both cases imperfections reduce the coincidence probability and in the limit of a totally imperfect PBS or PC it will go to zero. This is due to the fact that with increasing imperfections the PBS starts to separate photons with different polarisation not perfectly which leads to a mixture of photons with different polarisation in both channels that destroys the two-photon quantum interference. Increasing imperfections of the PC correspond to a non-perfect conversion of the polarisation in upper channel which leads to a reduced indistinguishability and thus a weakening of the two-photon quantum interference. Fig. 14(d) displays the change of the visibility as a function of the imperfection of the BS and the change of the maximum value in the coincidence probability as function of the imperfections of the PBS and the PC. In agreement with the above arguments, the visibility of the HOM dip

$$\nu = \frac{P_{b,c}^{\lambda,\lambda'}(\infty) - P_{b,c}^{\lambda,\lambda'}(0)}{P_{b,c}^{\lambda,\lambda'}(\infty)} \tag{25}$$

decreases to zero for a totally imperfect BS, whereas the maximum coincidence probabilities decrease from the ideal value of 0.5 towards zero with increasing imperfections of the PBS and the PC. From Fig. 14 it follows that the quantum interference is observed even for 25 % of imperfections in optical elements. The recently achieved fabrication technique allows holding losses in a few percent range (2-3 %) that makes expect a full experimental realisation of an on-chip interferometer in the nearest future.

IV. CONCLUSIONS

We have discussed advanced integrated circuits realised in $LiNbO_3$ for quantum optical applications. With a few basic components one gets a toolbox which can be used to design a variety of quantum circuits with different functionalities. We have shown, how such a circuit design can strongly benefit from developments of integrated components originally dedicated for applications in communication and sensing. Theoretical models for the description of the basic components have been developed. These models can be applied to design advanced circuits even for cases, where the performance of the individual components deviates from ideal functionality and predict quantum interference effects for a real experimental parameters. By this work we provide guidelines and modelling tools which should be helpful to pave the way towards the implementation of advanced integrated quantum circuits harnessing the potential of $LiNbO_3$.

ACKNOWLEDGEMENT

This work was funded by the Deutsche Forschungsgemeinschaft (DFG) via TRR 142/1, project C02. P. R. Sh. thanks the state of North Rhine-Westphalia for support by the *Landesprogramm für geschlechtergerechte Hochschulen.*

[1] A. Politi, Martin J. Cryan, J. G. Rarity, S. Yu, J. L. O'Brien, "Silica-on-Silicon Waveguide Quantum Circuits", Science 320, 646 (2008).

[2] A. Peruzzo, A. Laing, A. Politi, T. Rudolph, J.L. O'Brien, "Multimode quantum interference of photons in multiport integrated devices", Nature Comm. 2, 224 (2011).

[3] J. B. Spring, B. J. Metcalf, P. C. Humphreys, W. S. Kolthammer, Xian-Min Jin, M. Barbieri, A. Datta, N. Thomas-Peter, N. K. Langford, D. Kundys, J. C. Gates, B. J. Smith, P. G.R. Smith, I. A. Walmsley, "Boson Sampling on a Photonic Chip", Science 339, 798 (2012).

[4] A. Peruzzo, M. Lobino, J. C. F. Matthews, N. Matsuda, A. Politi, K. Poulios, X.-Q. Zhou, Y. Lahini, N. Ismail, K. Wörhoff, Y. Bromberg, Y. Silberberg, M. G. Thompson, J. L. O'Brien, "Quantum Walks of Correlated Photons", Science 329, 1500 (2010).

[5] A. Crespi, R. Osellame, R. Ramponi, V. Giovannetti, R. Fazio, L. Sansoni, F. De Nicola, F. Sciarrino, P. Mataloni, "Anderson localization of entangled photons in an integrated quantum walk", Nature Photonics 7, 322 (2013).

[6] S. Tanzilli, A. Martin, F. Kaiser, M. de Micheli, O. Alibart, D. B. Ostrowsky, "On the genesis and evolution of integrated quantum optics", Laser & Photonics Reviews 6, 115-143 (2012)

[7] J.L. O'Brien, B. Patton, M. Sasaki, J. Vučković, "Focus on integrated quantum optics", New J. Phys. 15, 035016 (2013).

[8] S. Bogdanov, M. Y. Shalaginov, A. Boltasseva, V. M. Shalaev, "Material platforms for integrated quantum photonics," Opt. Mater. Express 7, 111-132 (2017)

[9] D. S. Hum, M. M. Fejer, "Quasi-phase matching", Comptes Rendus Physique 8, 180198 (2007)

[10] S. Tanzilli, W. Tittel, H. De Riedmatten, H. Zbinden, P. Baldi, M. DeMicheli, D.B. Ostrowsky, N. Gisin, "PPLN waveguide for quantum communication" , Eur. Phys. J. D 18, 155 (2002)

[11] Y.-K. Jiang, A. Tomita, "Highly efficient polarization-entangled photon source using periodically-poled lithium niobate waveguides", Opt. Commun. 267, 278 (2006)

[12] T. Nosaka, B. K. Das, M. Fujimura, T. Suhara, "Cross-polarized twin photon generation device using quasi-phase matched $LiNbO_3$ waveguide" , IEEE Photon. Technol. Lett. 18, 124 (2006)

[13] T. Suhara, H. Okabe, M. Fujimura, "Generation of polarization-entangled photons by type-II quasi-phase-matched waveguide nonlinear-optic device", Photon. Technol. Lett. 19, 1093 (2007)

[14] A. Martin, V. Cristofori, P. Aboussouan, H. Herrmann, W. Sohler, D. B. Ostrowsky, O. Alibart, S. Tanzilli, "Integrated optical source of polarization entangled photons at 1310 nm", Opt. Exp. 17, 1033 (2009)

[15] G. Fujii, N. Namekata, M. Motoya, S. Kurimura, S. Inoue, "Bright narrowband source of photon pairs at optical telecommunication wavelengths using a type-II periodically-poled lithium niobate waveguide", Opt. Exp. 15, 12769 (2007)

[16] H. Herrmann, X. Yang, A. Thomas, A. Poppe, W. Sohler, C. Silberhorn "Post-selection free, integrated optical source of non-degenerate, polarization entangled photon pairs" Opt. Exp. 21, 27981 (2013)

[17] O. Alibart, V. d'Auria, M. de Micheli, F. Doutre, F. Kaiser, L. Labonte, T. Lunghi, E. Picholle, S. Tanzilli, "Quantum photonics at telecom wavelengths based on lithium niobate waveguides", J. Opt. 18, 104001 (2016)

[18] S. Krapick, H. Herrmann, V. Quiring, B. Brecht, H. Suche, C. Silberhorn, "An Efficient Integrated Two-Color Source for Heralded Single Photons", New J. Phys. 15, 033010 (2013)

[19] A. Martin, O. Alibart, M. De Micheli, D. B. Ostrowsky, S. Tanzilli, "A quantum relay chip based on telecommunication integrated optics technology", New J. Phys. 14, 025002 (2012)

[20] H. Jin, F.M. Liu, P. Xu, J.L. Xia, M.L. Zhong, Y. Yuan, J.W. Zhou, Y.X. Gong, W. Wang, S.N. Zhu, "On-Chip Generation and Manipulation of Entangled Photons Based on Reconfigurable Lithium-Niobate Waveguide Circuits", Phys. Rev. Lett. 113, 103601 (2014)

[21] W. Sohler, H. Hu, V. Quiring, C. Vannahme, H. Herrmann, D. Büchter, S. Reza, W. Grundkötter, S. Orlov, H. Suche , R. Nouroozi, Y. Min, "Integrated optical devices in lithium niobate", Optics & Photonics News 19, 24 (2008)

[22] G. J. Edwards, M. Lawrence, "A temperature-dependent dispersion equation for congruently grown lithium niobate", Opt. Quant. Electron. 16, 373 (1984)

[23] D. H. Jundt, "Temperature-dependent Sellmeier equation for the index of refraction, n_e, in congruent lithium niobate", Opt. Lett. 22, 1553 (1997)

[24] S. K. Korotky, W. J. Minford, L. L. Buhl, M. D. Divino, R. C. Alferness, "Mode size and method for estimating the propagation constant of single-mode Ti:$LiNbO_3$ strip waveguides", IEEE J. Quant. Electron. QE-18, 1796 (1982)

[25] C. K. Law, I. A. Walmsley, J. H. Eberly, "Continuous Frequency Entanglement: Effective Finite Hilbert Space and Entropy Control", Phys. Rev. Lett. 84, 23 (2000)

[26] V. G. Dmitriev, G. G. Gurzadyan, D. N. Nikogosyan, "Handbook of Nonlinear Optical Crystals", Springer (1999)

[27] E. Strake, G.P. Bava, I. Montrosset, "Guided modes of Ti:$LiNbO_3$ channel waveguides: a novel quasi-analytical technique in comparison with the scalar finite-element method", J. Lightwave Technol. 6, 1126 (1988)

[28] T. Suhara, M. Fujimura, "Waveguide Nonlinear-Optic Devices", Springer (2003)

[29] L. Bersiner, U. Hempelmann, E. Strake, "Numerical analysis of passive integrated optical polarization splitters: comparison of finite-element method and beam propagation method results", J. Opt. Soc. Am. B 8, 422-431 (1991)

[30] H. Kogelnik, R. V. Schmidt, "Switched directional couplers with alternating $\Delta\beta$", IEEE J. Quantum Electron. QE-12, 396-401 (1976)

[31] C. Y. Huang, C. H. Lin, Y.H. Shen, "Electro-optic Ti:PPLN waveguide as efficient optical wavelength filter and polarization mode converter", Opt. Exp. 15, 2548 (2007)

[32] N. Moeini, H. Herrmann, R. Ricken, V. Quiring, W. Sohler, "Electro-optic polarization controller with Ti:PPLN channel waveguides", Proc. European Conference on Integrated Optics ECIO 2010, Cambridge , paper

FrD4 (2010)
[33] F. Heismann, R. C. Alferness, "Wavelength-Tunable Electrooptic Polarization Conversion in Birefringent Waveguides", IEEE Journal of Quantum Electronics QE-24, NO 1 (1988).